Supporting Information for

"Investigating trends in actinide covalency and magnetism with $^{35/37}$Cl SSNMR spectroscopy and first-principles calculations"

Adam R. Altenhof[1,*,†], Karla A. Erickson[2], Daniel A. Rehn[3], Taylor V. Fetrow[4], Ann E. Mattsson[3], Marisa J. Monreal[5], and Harris E. Mason[5,*]

1. MPA-Q, Los Alamos National Laboratory, Los Alamos, NM 87545, USA
2. C-CDE, Los Alamos National Laboratory, Los Alamos, NM 87545, USA
3. XCP-5, Los Alamos National Laboratory, Los Alamos, NM 87545, USA
4. Sigma-1, Los Alamos National Laboratory, Los Alamos, NM 87545, USA
5. C-IIAC, Los Alamos National Laboratory, Los Alamos, NM 87545, USA

*Author to whom correspondence should be addressed.
†Current Address: Geothermal Energy and Geofluids Group, Department of Earth and Planetary Sciences, ETH Zürich, Zürich 8001, Switzerland
E-mail: adam.altenhof@eaps.ethz.ch, hmason@lanl.gov

Table of Contents:

Table S1. Experimental Parameters for ^{35}Cl WURST-CPMG Experiments in **Fig. 1**

	$LaCl_3$	$NdCl_3$	UCl_3	UCl_4
Transmitter Frequency (MHz)	39.146	39.186	39.171	39.116
Number of Averages	32	8192	131072	65536
Recycle Delay (s)	15	0.4	0.09	0.1
Experimental Time (min)	8.0	54.6	218.5	109.2
Dwell Time (μs)	1.0	1.0	1.0	1.0
Number of CPMG Loops (N)	90	8	4	20
Spin Echo length, τ_{SE} (μs)	260	700	350	250
WURST Pulse Amplitude (kHz)	6.52	9.96	16.94	21.13
WURST Pulse Width (μs)	100	50	50	50
WURST Sweepwidth (kHz)	500	800	600	1000

Table S2. Experimental Parameters for ^{37}Cl WURST-CPMG Experiments in **Fig. 1**

	$LaCl_3$	$NdCl_3$	UCl_3	UCl_4
Transmitter Frequency (MHz)	32.617	32.617	32.617	32.617
Number of Averages	1024	131072	262144	262144
Recycle Delay (s)	17	0.1	0.1	0.1
Experimental Time (hr)	4.8	3.6	7.3	7.3
Dwell Time (μs)	1.0	1.0	1.0	1.0
Number of CPMG Loops (N)	100*	10	6	20
Spin Echo length, τ_{SE} (μs)	250	700	250	250
WURST Pulse Amplitude (kHz)	17.86	17.86	17.86	17.86
WURST Pulse Width (μs)	50	50	50	50
WURST Sweepwidth (kHz)	500	800	700	1000

*512 echoes were measured to determine the $LaCl_3$ ^{37}Cl T_2^{eff}

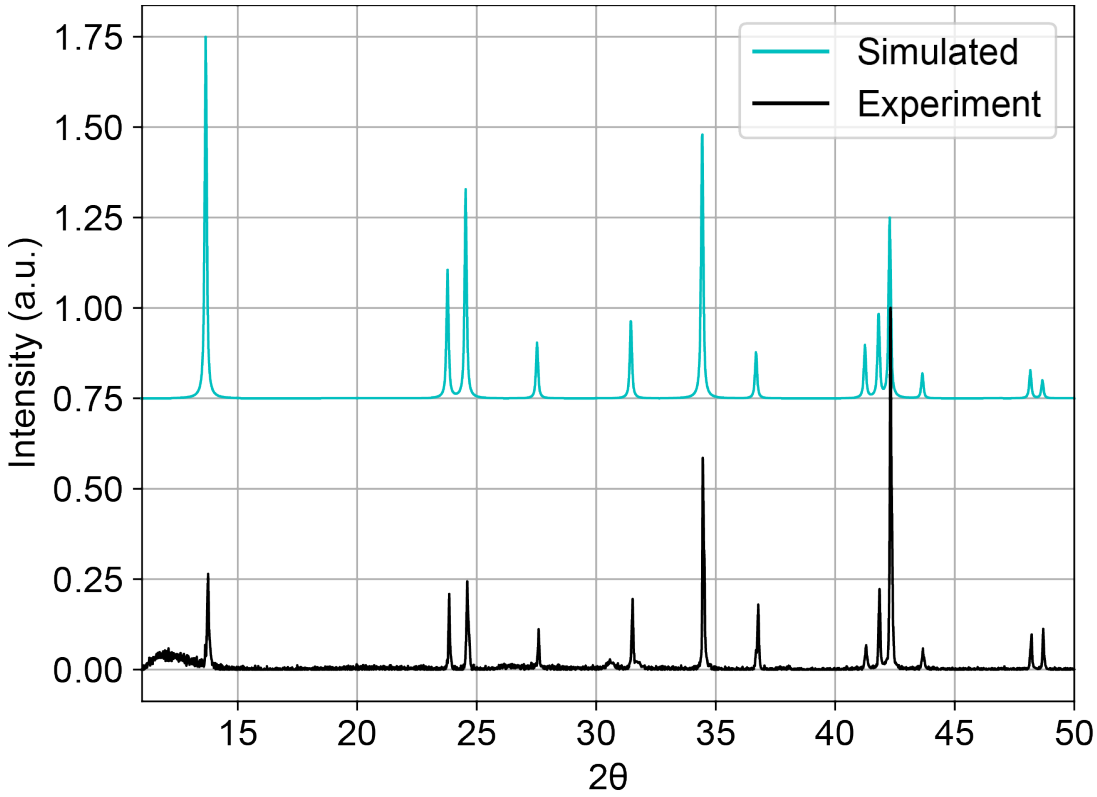

Figure S1. Powder Xray diffraction patterns of $LaCl_3$.[1]

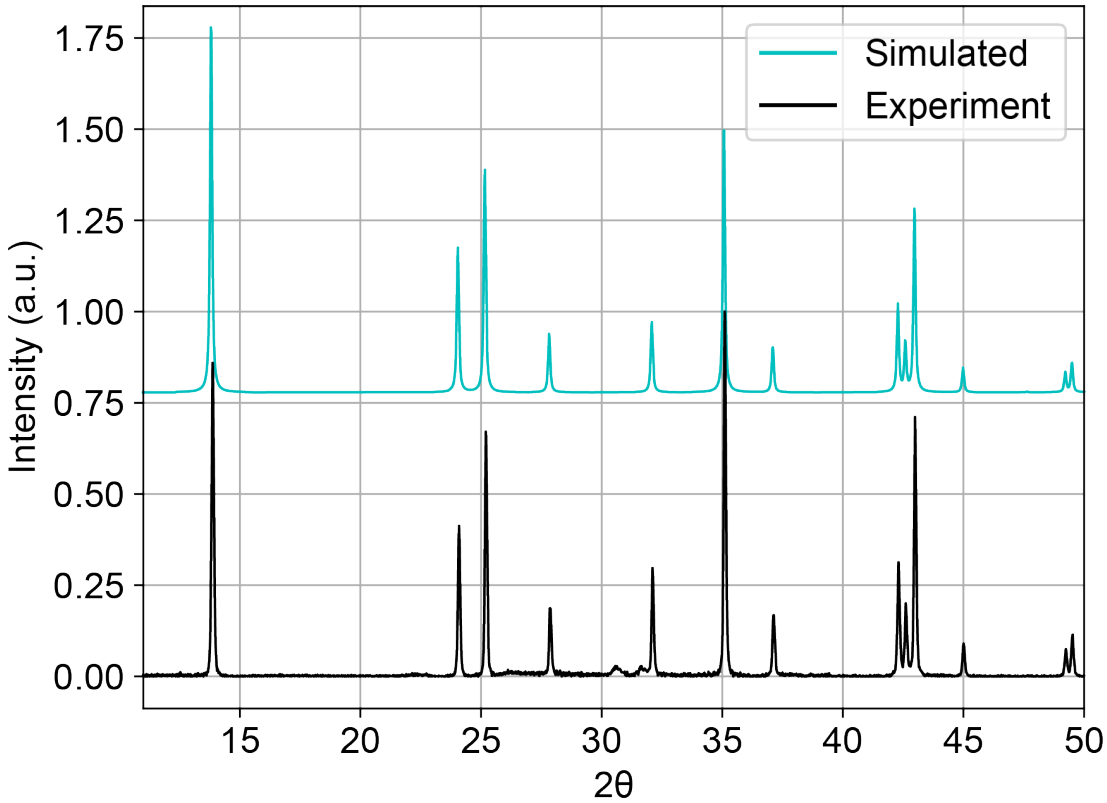

Figure S2. Powder Xray diffraction patterns of $NdCl_3$.[1]

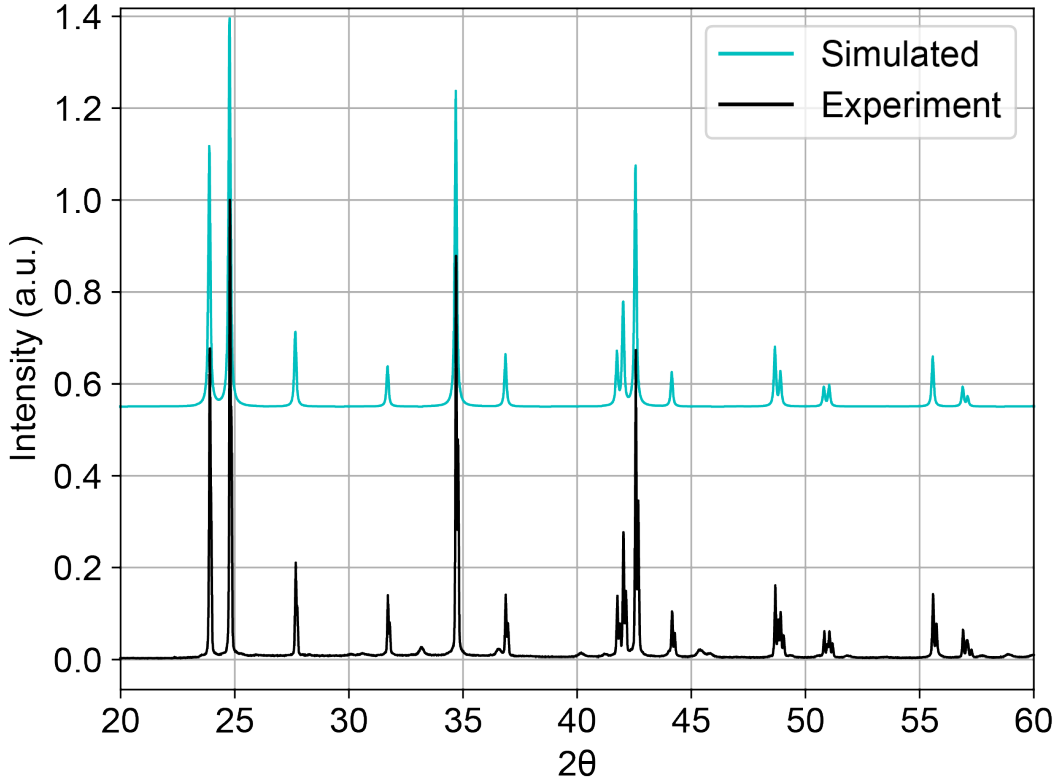

Figure S3. Powder Xray diffraction patterns of UCl_3.[2]

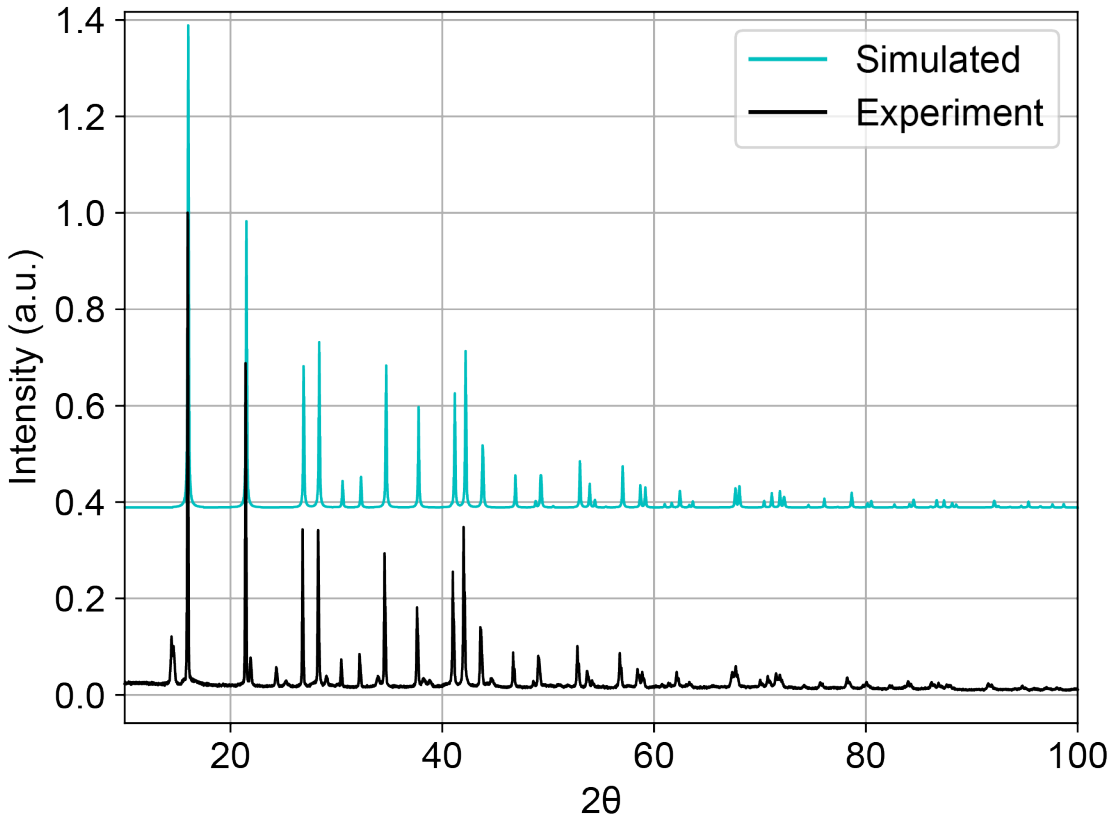

Figure S4. Powder Xray diffraction patterns of UCl_4.[3]

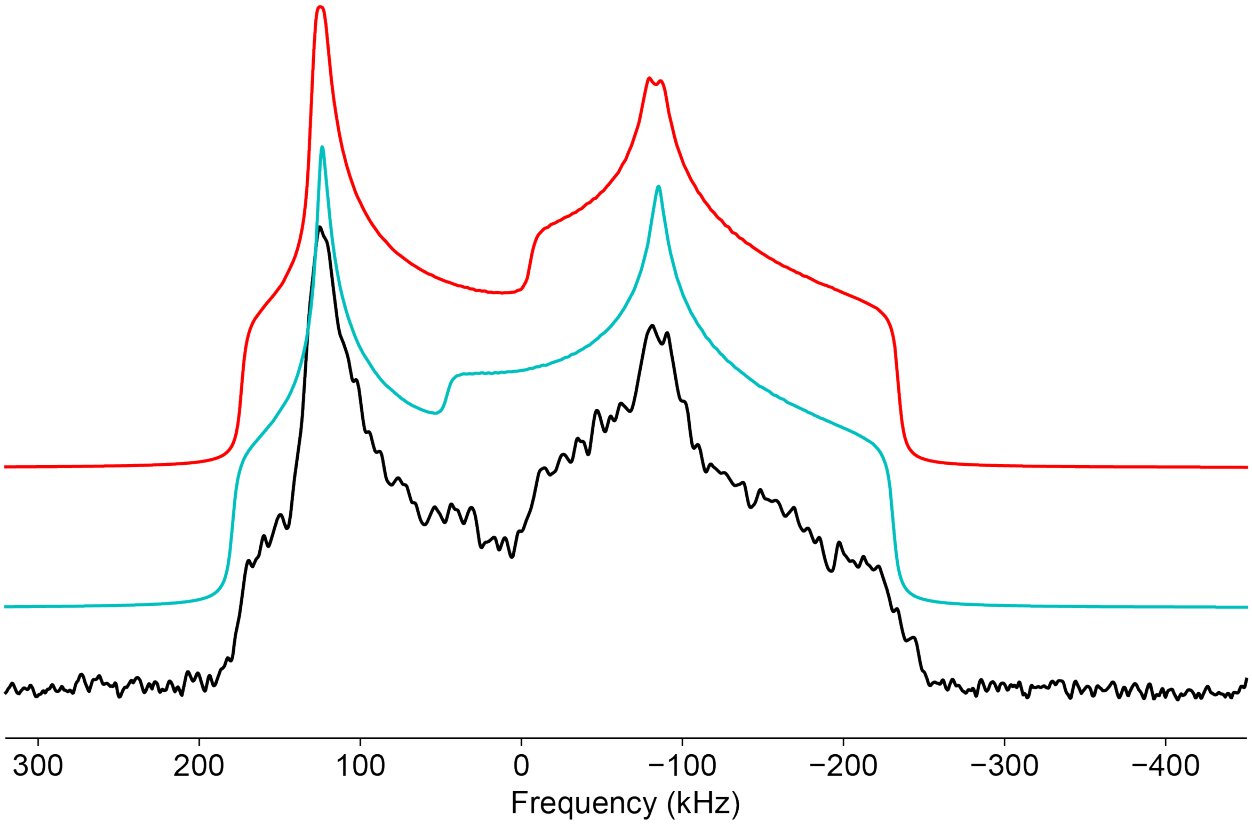

Figure S5. ^{35}Cl NMR spectra of $NdCl_3$ acquired experimentally (black) and simulated with tensor parameters from a best fit including only the EFG parameters and δ_{iso} (blue) or with the EFG and SA parameters (red). Simulated fitted spectra generated in ssNake. The fit in blue yielded C_Q = 9.63 MHz, η_Q = 0.369, and δ_{iso} = 996.6 ppm. The fit in red is summarized in **Table 1**.

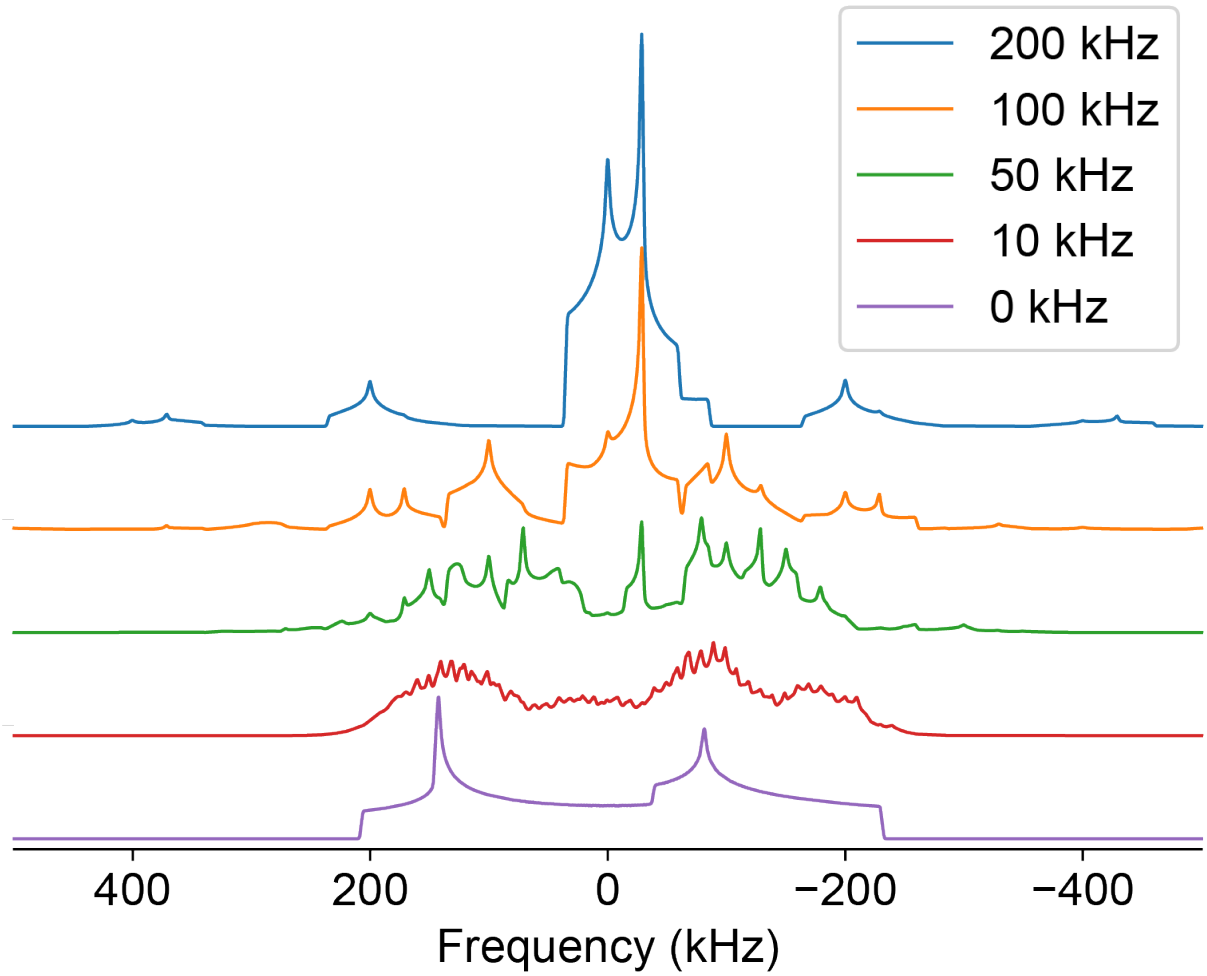

Figure S6. ^{35}Cl NMR spectra of UCl_3 simulated in SIMPSON using tensor parameters from **Table 1**. The spectrum is simulated under static conditions (0 kHz spin rate; purple) and MAS using varied spinning rates as indicated in the legend. 46367 tensor orientations are sampled according to the ZCW averaging scheme and 64 γ angles are used.

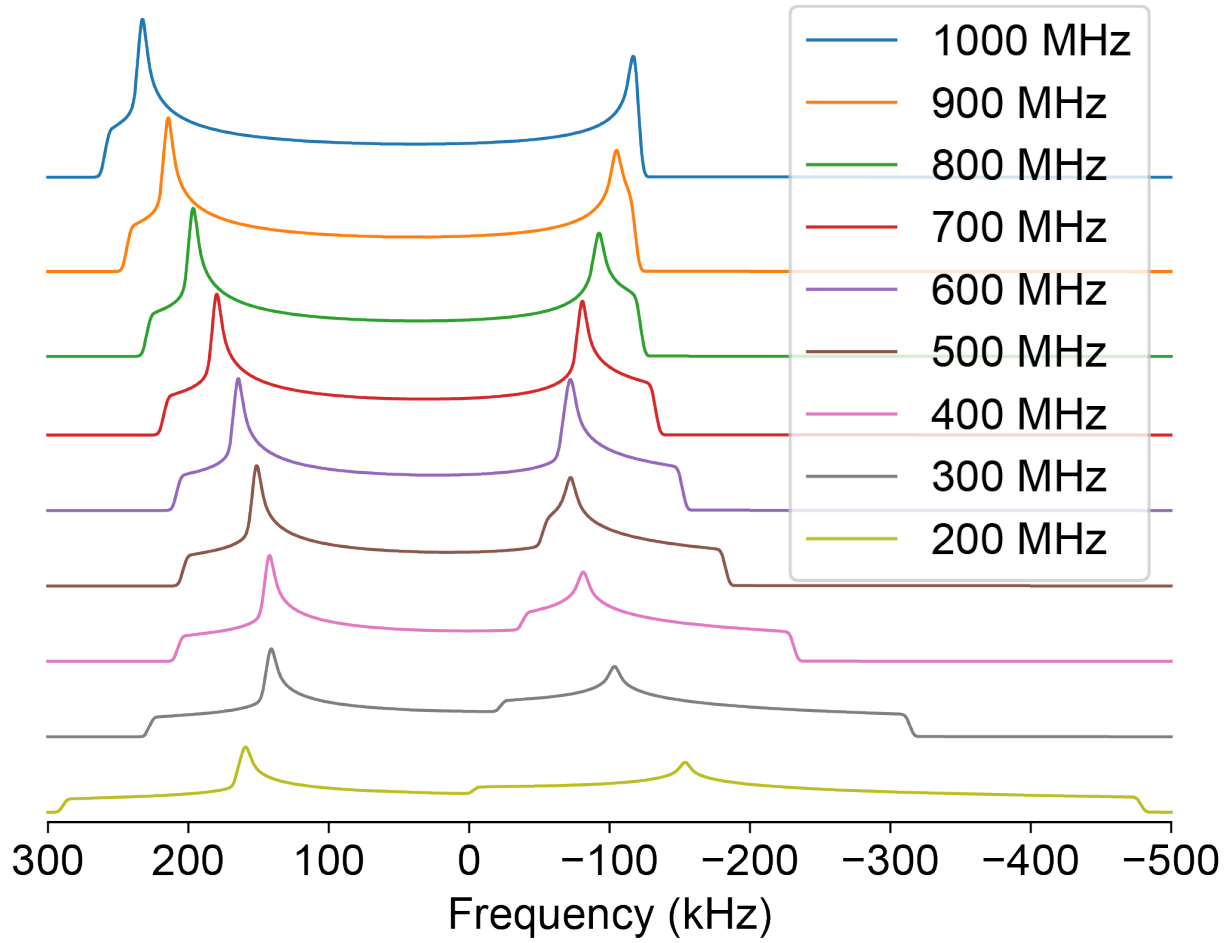

Figure S7. ^{35}Cl NMR spectra of UCl_3 simulated in SIMPSON using tensor parameters from **Table 1**. The spectrum is simulated under static conditions using varied magnetic field strengths indicated in the legend as the corresponding ^{1}H Larmor frequency. 46367 tensor orientations are sampled according to the ZCW averaging scheme.

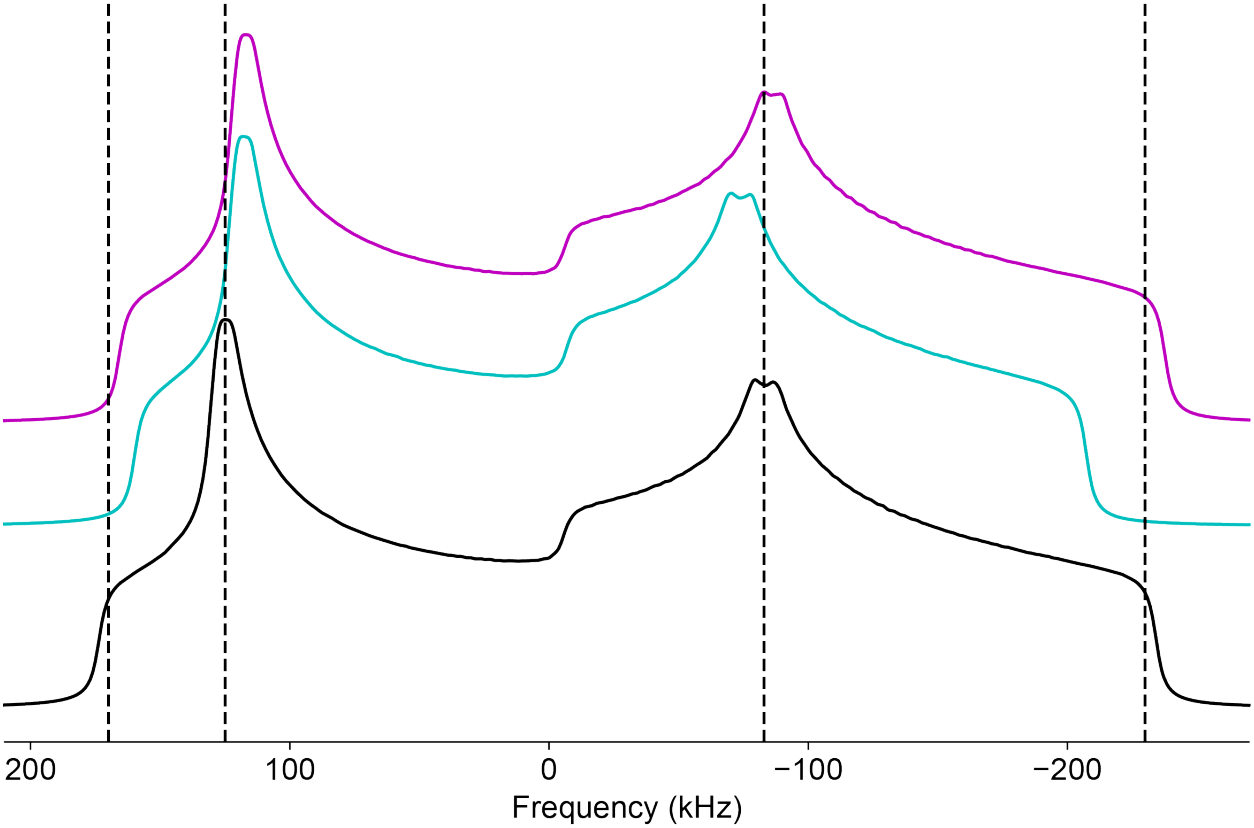

Figure S8. ^{35}Cl NMR spectra of $NdCl_3$ simulated in ssNake using tensor parameters from **Table 1** (black) and simulated using the same parameters expect the C_Q is set to 8.50 MHz (blue) rather than 8.99 MHz. Another spectrum is simulated using the same parameters as **Table 1** expect the δ_{11} and δ_{22} components of the SA tensor are both decreased by 200 ppm (magenta). The blue spectrum decreases in total pattern breadth and shows a shift it all discernable discontinuities relative to the black one (as indicated by dashed lines). The magenta spectrum shows a slight shift in the high-frequency discontinuities, a small shift in the low-frequency horn discontinuity, and a negligible shift in the low-frequency edge of the pattern.

Further details on DFT calculations

In this study, all the calculations presented in the main text were performed on the room temperature crystal structures without structural relaxation. A prior DFT investigation of inorganic materials containing ^{27}Al and ^{7}Li has indicated that structural relaxation has a negligible effect on the final calculated EFG tensors of materials not containing hydrogen.[4] Furthermore, the primary use of DFT+*U* in this study is to investigate the amount of electron localization on the metal and not structural refinement.

Baseline parameters for the generalized gradient approximation (GGA), plane-wave cutoff energy, k-point mesh, and energy convergence were determined on the diamagnetic $LaCl_3$ system. In this system, both ^{137}La and $^{35/37}$Cl quadrupole tensors have been experimentally determined so the accuracy of the model was assessed using the root mean squared EFG distance metric (Γ_{RMS}) as proposed in Holmes et al.[5]

$$\Gamma_m = \left(\frac{1}{15}[3\Delta_{11}^2 + 3\Delta_{22}^2 + 3\Delta_{33}^2 + 2\Delta_{11}\Delta_{22} + 2\Delta_{11}\Delta_{33} + 2\Delta_{22}\Delta_{33}]\right)^{1/2} \quad (1)$$

$$\Delta_{kk} = \left|V_{kk}^{m,calc}\right| - \left|V_{kk}^{m,exp}\right| \quad (2)$$

$$\Gamma_{RMS} = \frac{1}{M}\sum_m \Gamma_m^2 \quad (3)$$

Where $V_{kk}^{m,calc}$ and $V_{kk}^{m,exp}$ are the principal axis components of the EFG tensor V calculated from DFT and experimental measured, respectively. The Γ_m was used for all other optimizations where only the $^{35/37}$Cl experimental EFG tensors are available. The best parameters were determined to be the standard Perdew-Burke-Ernzerhof (PBE) GGA with 0.25 Å^{-1} k-point spacing, a 500 eV plane-wave cutoff energy, and a 1×10^{-8} eV energy convergence was determined to produce the best match to experimental results in $LaCl_3$ in the absence of DFT+U. Given the presence of relativistic effects in La, DFT+U was also applied to the 5d orbitals in

$LaCl_3$ in the absence of spin polarization. A U_{eff} value of 3.0 eV was determined to give the smallest Γ_{RMS} (**Figure S9, top left**). Changing U_{eff} has a significant effect on the $^{35/37}Cl$ EFG tensor (**Figure S9, top right**), but a minor effect on the ^{137}La EFG tensor (**Figure S9, bottom left**)

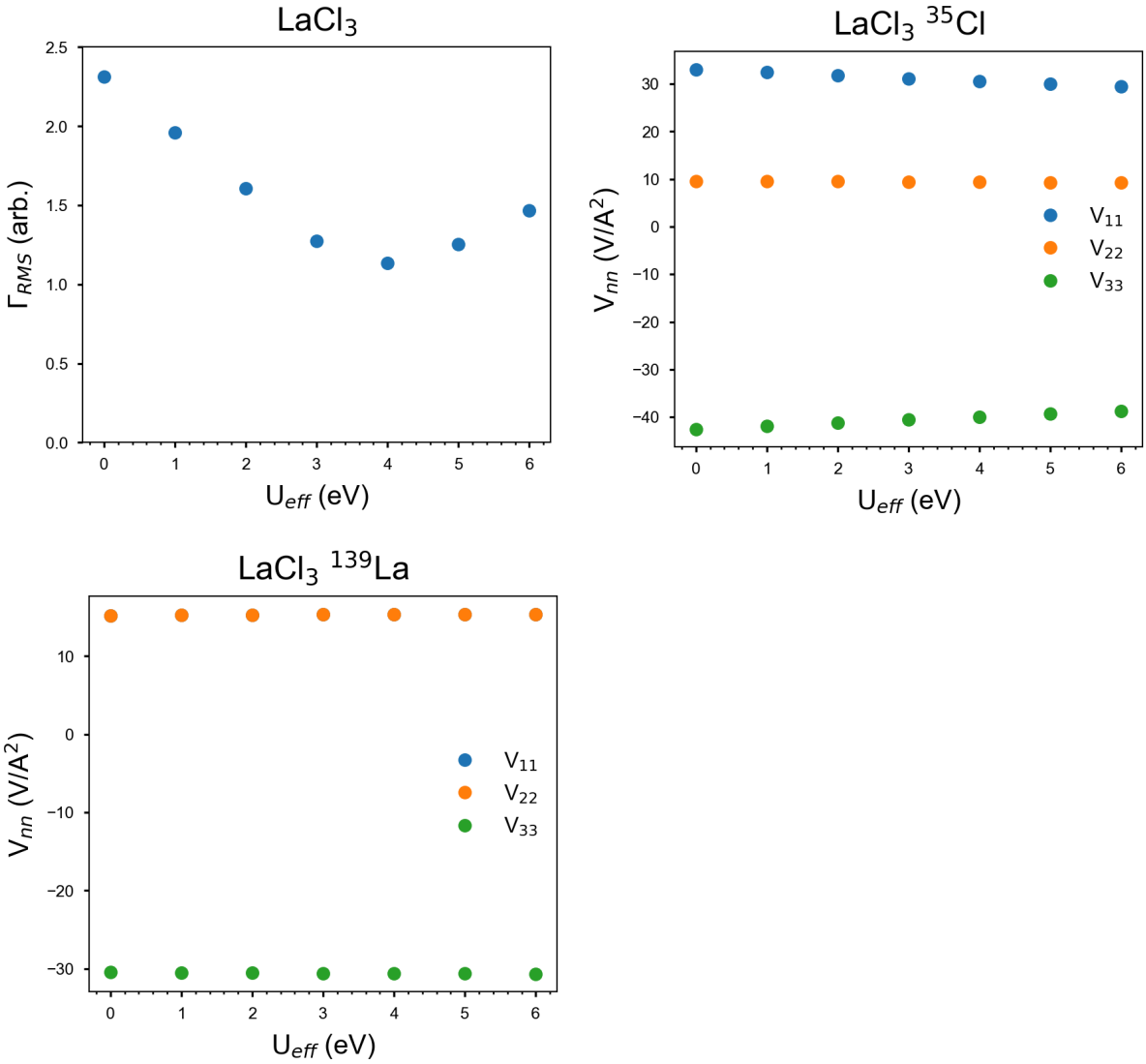

Figure S9: Calculated root mean squared EFG distance parameter (Γ_{RMS}) for $LaCl_3$ as a function of U_{eff} (top left panel) and the corresponding principle components for the ^{35}Cl (top right) and ^{139}La (bottom left) EFG tensors.

The influence of changing U_{eff} and spin orbit coupling (SO) was investigated on each of the three paramagnetic materials. For the purposes of optimizing the initial U_{eff}, the calculations were

initially performed without SO. For SO calculations, the initial U_{eff} value determined in the absence of SO was used as a starting point. The SO calculations were initiated from converged self-consistent calculations with SO with the crystal symmetry turned off. The results for the $+U$ calibration is shown in **Figure S9**. The application of SO to the UCl_4 system in addition to $+U$ has no effect on the calculated EFG tensors, but largest effect is decreasing the value of U_{eff} required to obtain a suitable match to the experimental results, while applying SO to UCl_3 has a negligible effect on the calculated EFG tensor and the applied U_{eff} values (**Table S3**). Additional calculations using HSE06 hybrid functionals were also performed for UCl_3 using the default values for the exchange parameters. These calculations were difficult to converge and did not converge below an energy difference of 10^{-4} eV and produced similar results for the calculated EFG tensor (**Table S3**)

Table S3: Calculated ^{35}Cl EFG Tensor Parameters with and without spin orbit (SO) coupling for UCl_3 and UCl_4 and those calculated for UCl_3 using HSE06 hybrid functionals.

Compound	Calculation	U_{eff} (eV)	C_Q (MHz)	η
UCl_3	DFT+U	6.0	9.25	0.58
UCl_3	DFT+U+SO	6.0	9.27	0.58
UCl_3	HSE06	N/A	9.14	0.54
UCl_4	DFT+U	5.0	-11.99	0.31
UCl_4	DFT+U+SO	4.0	-11.99	0.33

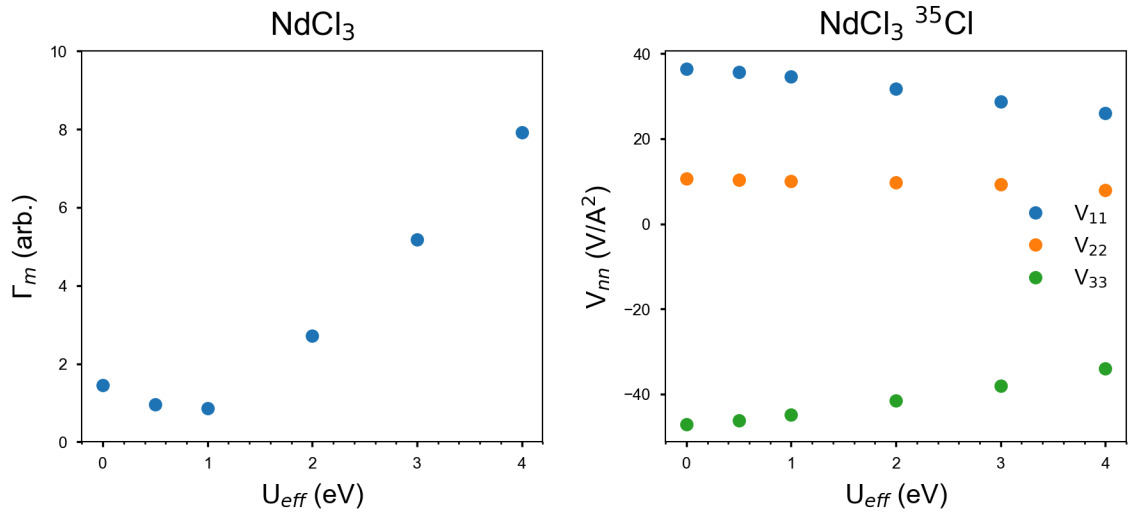

Figure S10: Calculated ^{35}Cl C_Q values as a function of the applied U_{eff} correction (left panel) and the corresponding EFG distance matric as compared to experiment (right panel) for $NdCl_3$.

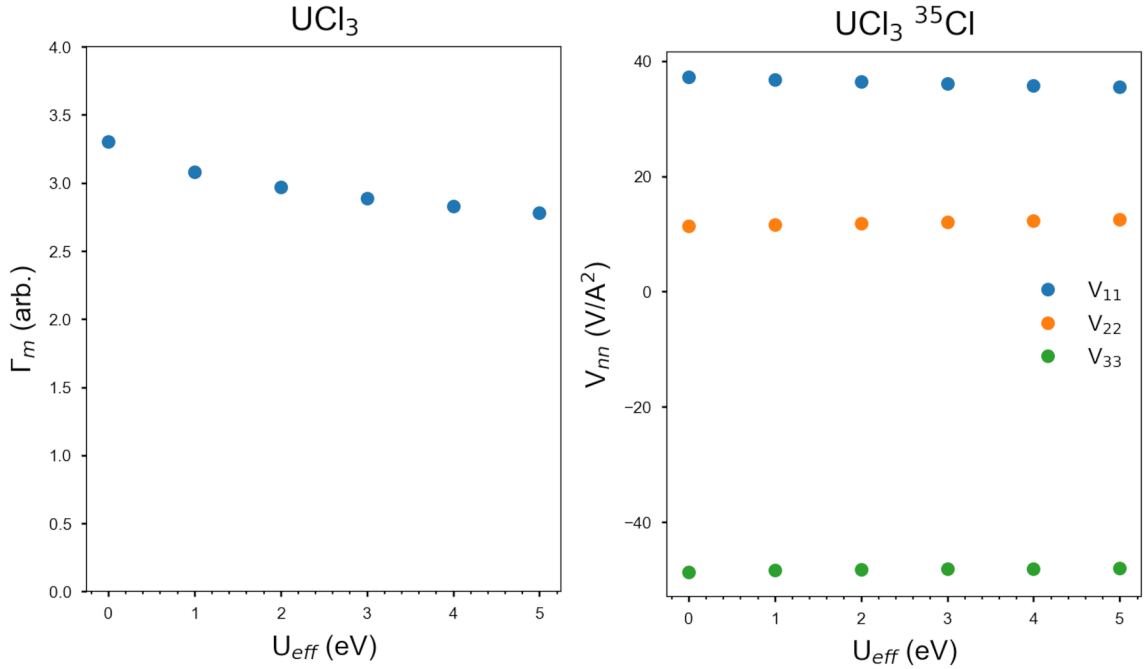

Figure S11: Calculated ^{35}Cl C_Q values as a function of the applied U_{eff} correction (left panel) and the corresponding EFG distance matric as compared to experiment (right panel) for UCl_3.

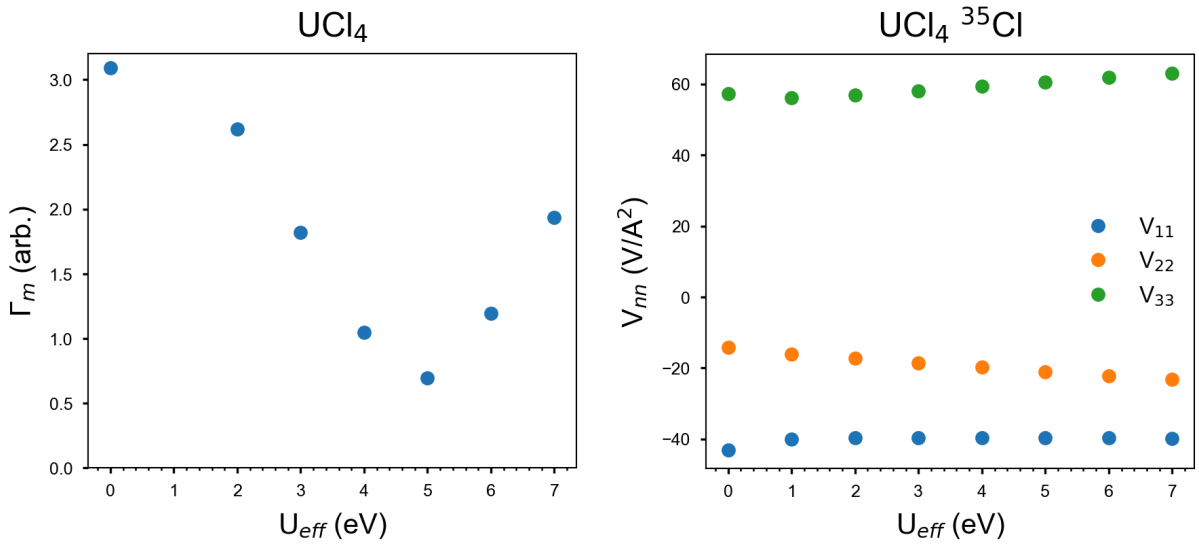

Figure S12: Calculated ^{35}Cl C_Q values as a function of the applied U_{eff} correction (left panel) and the corresponding EFG distance matric as compared to experiment (right panel) for UCl_4.

Application of SO to $NdCl_3$ produces qualitatively incorrect results compared to the experimental results. In VASP, all non-collinear magnetism calculations are recommended be performed with and without the crystal symmetry turned on. For the uranium-chlorides, the results of SO calculations without crystal symmetry produce equivalent EFG tensors for all Cl sites in the material which is expected for their crystal structure. The same would be expected for $NdCl_3$. However, the Cl sites are inequivalent and differ significantly in magnitude with C_Q ranging from 7 to 10 MHz. Attempts to vary the U_{eff} and other parameters produce the same results.

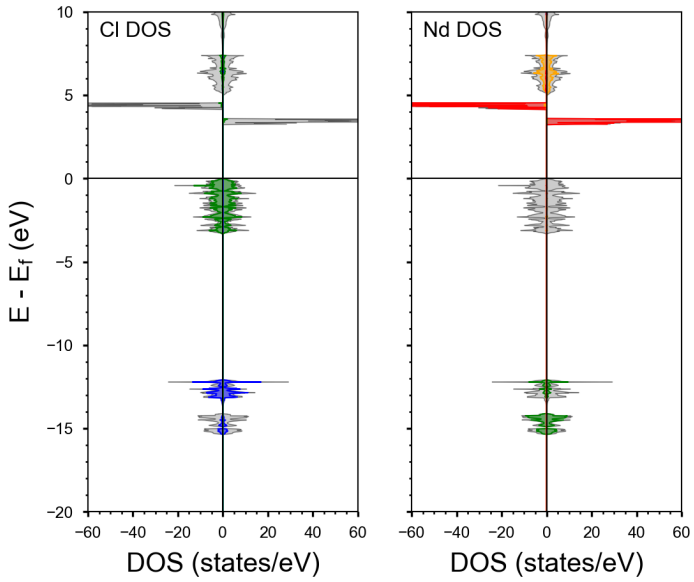

Figure S13. Density of states (DOS) calculated for $NdCl_3$ with the +U applied to the neodymium 4f orbitals. The full DOS is show in grey and has been band decomposed for chlorine (left) and neodymium (right). Red, orange, green, and blue correspond to the f, d, p and s orbitals, respectively.

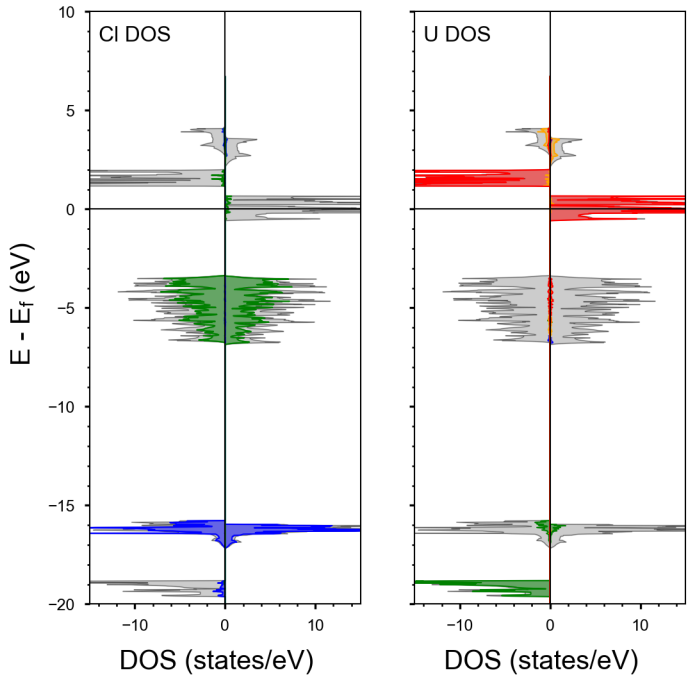

Figure S14. Density of states (DOS) calculated for UCl_3 with the +U applied to the uranium 6d orbitals. The full DOS is show in grey and has been band decomposed for chlorine (left) and uranium (right). Red, orange, green, and blue correspond to the f, d, p and s orbitals, respectively.

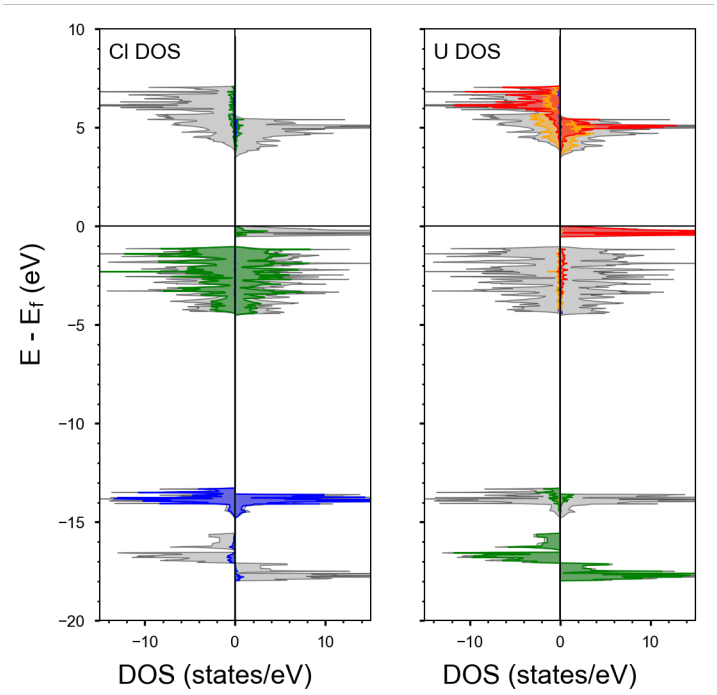

Figure S15. Density of states (DOS) calculated for UCl_3 with the +U applied to the uranium 5f orbitals. The full DOS is show in grey and has been band decomposed for chlorine (left) and uranium (right). Red, orange, green, and blue correspond to the f, d, p and s orbitals, respectively.

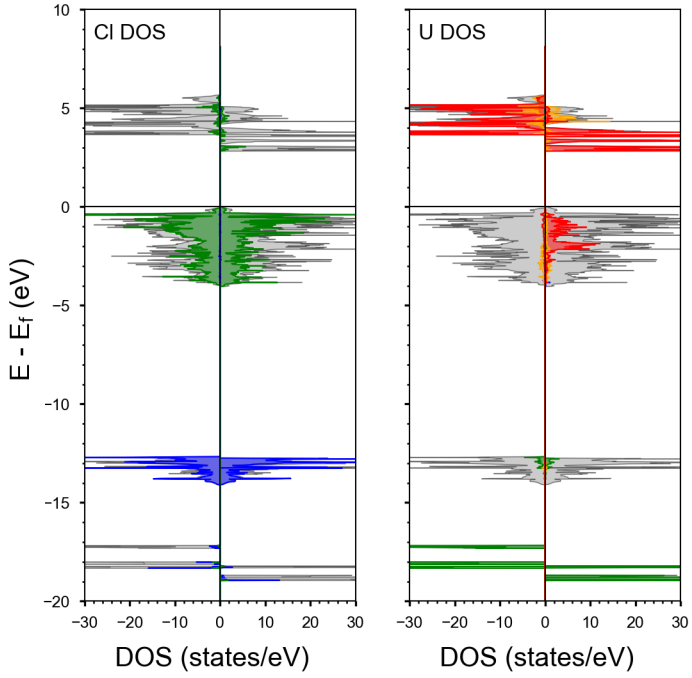

Figure S16. Density of states (DOS) calculated for UCl_4 with the +U applied to the uranium 5f orbitals. The full DOS is show in grey and has been band decomposed for chlorine (left) and uranium (right). Red, orange, green, and blue correspond to the f, d, p and s orbitals, respectively.

Additional discussion of DFT calculations and chemical shifts

As noted in the main text, additional calculations were performed on UCl_3 where the $+U$ correction was applied to the 6*d* orbitals of uranium instead of the 5*f* orbitals. Placing this correction on the 6*d* orbitals produces a near exact match to the experimentally determined EFG parameters (**Table 1**). Closer examination of the acquired density of states (DOS) illustrates the issues with the 6d $+U$ (**Figure S10)** model compared to the 5*f* $+U$ model (**Figure S11**). The DOS for the case without $+U$ and that with 6d $+U$ show occupied 5*f* orbitals at the Fermi level which suggest a metallic character for the material which is a known insulator. When the correction is instead applied to the 5*f* orbitals, the expected band gap forms correctly predicting an insulating material. Contrastingly, the DOS for UCl_4 $5f + U$ model produces a bandgap in the DOS and hence both predicts the right EFG parameters and electronic state. These results could hint at the inability of scalar relativistic methods to fully describe actinide systems, but the effects are comparatively minor. More work is required with other DFT methods (*e.g.*, those based on Dirac's equation) to determine the impact of these effects. Examination of the DFT results must consider the full constellation of model results instead of relying solely on the match to experimental results.

The diamagnetic contribution to the chemical shifts was also calculated using the Gauge Including Projector Augmented Waves (GIPAW) method in VASP. In addition to the chlorides discussed in the main text, the chemical shifts of a series of 15 anhydrous chloride salts with literature values of their ^{35}Cl chemical shifts were also calculated to calibrate and correct the VASP calculated diamagnetic chemical shifts (**Table S4** and **Figure S17**). Each calculation was performed with a 500 eV cutoff energy, a 0.25 $Å^{-1}$ k-point spacing and a 1×10^{-8} eV convergence

criterion. The original unrelaxed crystal structures were used in every case. The compounds were chosen such that their literature reported chemical shifts ranged from –50 to 800 ppm which brackets the diamagnetic shifts calculated for the metal chlorides studied here.

The corrected DFT calculated diamagnetic shifts were used with the calculated hyperfine tensors and literature reported values of the g-tensors (**Table S5**) to calculate the shift anisotropy of the compounds studied here. The contributions to the ^{35}Cl isotropic and anisotropic chemical shifts were decomposed in terms of their diamagnetic, Fermi contact, and psuedocontact shifts (**Table S6**). The Fermi contact and psuedocontact shifts were further decomposed to illustrate the influence of the experimentally measured anisotropic *g*-tensor. Following the notation of Pigliapochi et al,[6] these terms are the free electron *g*-value (g_e, 2.002319), the isotropic shift relative to the free electron value (Δg^{iso}), and the anisotropic portion of the *g*-tensor (**Δg**). Importantly, the calculation of the final term was calculated as the weighted average over all the chlorine sites using the raw un-diagonalized chemical shift tensors produced by the VASP calculations since they have a different orientation with respect to the *g*-tensor. In every case, the *g*-tensors were aligned with the z-axis of the metal atom.

Table S4: DFT Calculated and literature reported experimental chemical shifts for a series of anhydrous metal chloride salts

Compound	δ_{iso} EXP (ppm)	δ_{iso} DFT	Ref
NaCl	-49.73	87.4	(7)
AgCl	-12.82	163.0	(7)
KCl	0.00	176.6	(7)
LiCl	1.31	141.0	(7)
RbCl	41.13	194.4	(7)
$MgCl_2$	131.0	77.5	(8)
$CaCl_2$	105.8	320.0	(8)
CsCl	106.0	326.4	(9)
$SnCl_2$	137.3 515.0	367.2 446.3	(10)

$GaCl_2$	200 200	348.0 343.1	(11)
$NbCl_5$	250 850 990	487.6 924.3 1075.9	(12)
$AlCl_3$	325 325	432.8 437.4	
$WOCl_4$	620	798.3	(12)
$MoOCl_4$	235 650 800 950	706.5 996.7 1038.9 1049.7	(12)
WCl_6	800	964.9	(12)

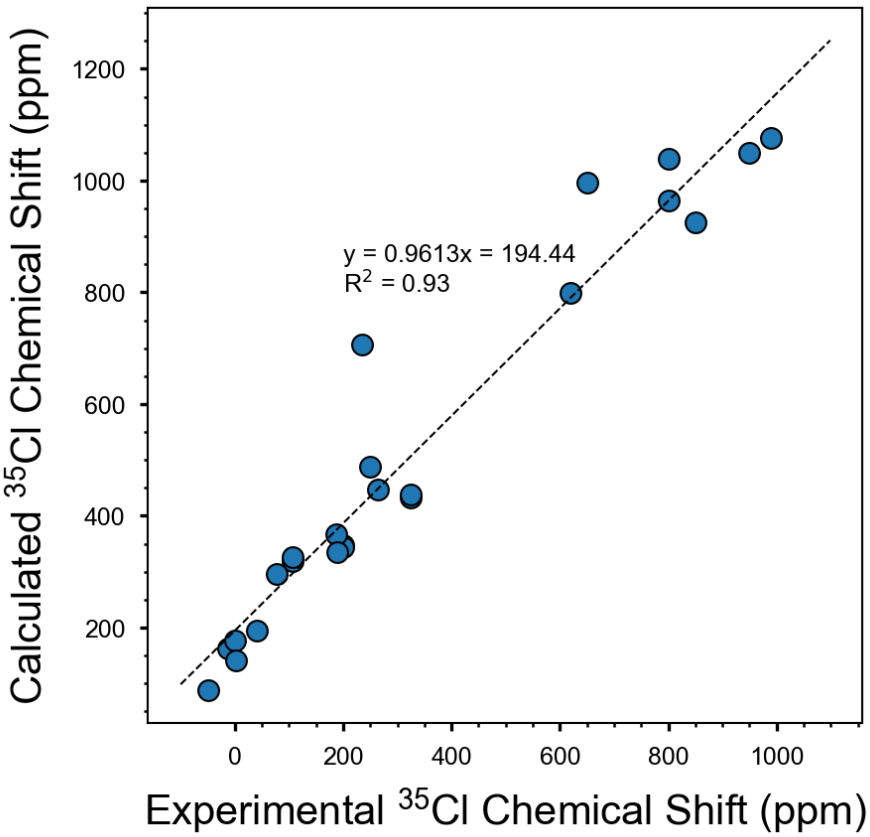

Figure S17: DFT Calculated versus experimental chemical shifts and corresponding linear fit for the 15 chlorides presented in **Table S4**.

Table S5: Mean DFT calculated hyperfine tensor values and experimental g-tensors.

	A_{iso} (MHz)	A_{xx} (MHz)	A_{yy} (MHz)	A_{ZZ} (MHz)	$g_{\perp}$	$g_{\parallel}$	Ref.
$NdCl_3$	-0.375	0.106	-0.237	0.132	1.653[†]	2.63[†]	(12)
UCl_3	-0.187	-0.173	0.230	-0.060	-1.520[‡]	-4.153[‡]	(13)
UCl_4	0.267	-0.08	0.236	-0.153	-0.1[‡,*]	-5.60[‡,*]	(14)

[†]Reported for Nd^{3+} in a YCl_3 matrix
[‡]Negative values for the g-tensor were required to match the experimental chemical shift
[*]Reported for U^{4+} in CaF_2.

Table S6: Comparison of the different contributions to the DFT calculated chemical shifts

	Orbital			Contact						Dipolar					
				g_eA^{FC}			ΔgA^{FC}			g_eA^{dip}			ΔgA^{FC}		
	δ_{iso} (ppm)	Ω (ppm)	κ	δ_{iso}	Ω (ppm)	κ	δ_{iso} (ppm)	Ω (ppm)	κ	δ_{iso} (ppm)	Ω (ppm)	κ	δ_{iso} (ppm)	Ω (ppm)	K
$NdCl_3$	482.7	1660	1.0	1374	0	—	-16.2	670.8	0.07	0	1451	1.0	-26.21	109.7	-0.43
UCl_3	216.6	103.6	0.64	1797	0	—	-353.7	2359.8	0.45	0	825	-0.98	-79.9	521.7	0.08
UCl_4	524.0	457.3	-1.0	-875	0	—	-88.43	2491	-1.0	0	484	0.07	0.61	507	-0.20

References

(1) Morosin, B. *J. Chem. Phys.* **1968**, *49*, 3007–3012.
(2) Taylor, J. C.; Wilson, P. W. *Acta Crystallogr. Sect. B Struct. Crystallogr. Cryst. Chem.* **1974**, *30*, 2803–2805.
(3) Taylor, J. C.; Wilson, P. W. *Acta Crystallogr. Sect. B Struct. Crystallogr. Cryst. Chem.* **1973**, *29*, 1942–1944.
(4) Valenzuela Reina, J.; Civaia, F.; Harper, A. F.; Scheurer, C.; Köcher, S. S. *Faraday Discuss.* **2025**, *255*, 266–287.
(5) Holmes, S. T.; Schurko, R. W. *J. Phys. Chem. C* **2018**, *122*, 1809–1820.
(6) Pigliapochi, R.; Pell, A. J.; Seymour, I. D.; Grey, C. P.; Ceresoli, D.; Kaupp, M. *Phys. Rev. B* **2017**, *95*, 054412.
(7) Bryce, D. L.; Sward, G. D. *Magn. Res. Chem.* **2006**, *44*, 409–450.
(8) Blaakmeer, E. S.; Antinucci, G.; Buscio, V.; van Eck, E. R. H.; Kentgens, A. P. M. *Phys. Chem. C.* **2016**, *120*, 6063–6074.
(9) Widdlefield, C. M.; Bryce, D. L.; *Can. J. Chem.* **2011**, *89*, 754–763.
(10) Lucier, B. E. G.; Tershikh, V. V.; Gui, J.; Bourque, J. L.; McOnie, S. L.; Ripmeester, J. A.; Huang, Y.; Baines, K. M. *Inorg. Chem.* **2020**, *59*, 13651–13670.
(11) Chapman, R. P.; Bryce, D. L. *Phys. Chem. Chem. Phys.* **2009**, *11*, 6987–6998.
(12) O'Keefe, C. A.; Johnston, K. E.; Sutter, K.; Autschbach, J.; Delevoye, L.; Popo, N.; Taou, M.; Oudatchin, K.; Schurko, R. W. *Inorg. Chem.* **2014**, *53*, 9581–9597.
(13) Garton, G.; Hutchings, T.; Shore, R.; Wolf, W. P. *J. Chem. Phys.***1964**, *41*, 1970–1974.
(14) Hutchison, C. A.; Llewellyn, P. M., Wong, E., Dorian, P. *Phys. Rev.* **1956**, 292
(15) Lupei, V.; Stoicescu, C.; *J. Phys. C:. Solid State Phys.* **1979**, *12*, 4585–4590.